Thermal conductance of interfaces with amorphous SiO_2 measured by time-resolved magneto-optic Kerr-effect thermometry

Judith Kimling,[1,*] André Philippi-Kobs,[2,†] Jonathan Jacobsohn,[2] Hans Peter Oepen,[2] and David G. Cahill[1]

[1]*Department of Materials Science and Engineering and the Frederick Seitz Materials Research Laboratory, University of Illinois at Urbana-Champaign, Urbana, Illinois 61801, USA*

[2]*Institut für Nanostruktur- und Festkörperphysik, Universität Hamburg, Jungiusstraße 11, 20355 Hamburg, Germany*

(Received 6 December 2016; revised manuscript received 28 March 2017; published 22 May 2017)

We use time-resolved magneto-optic Kerr effect and ultrathin Co/Pt transducer films to perform thermal-transport experiments with higher sensitivity and greater time resolution than typically available in studies of interfacial thermal transport by time-domain thermoreflectance. We measure the interface conductance between Pt and amorphous SiO_2 using Pt/Co/Pt ferromagnetic transducer films with thicknesses between 4.2 and 8.2 nm and find an average value of $G_{Pt} \approx 0.3$ GW m^{-2} K^{-1}. This result demonstrates that interfaces between metals and amorphous dielectrics can have a conductance corresponding to Kapitza lengths of the order of 4 nm, and are thus of relevance when engineering nanoscale devices. For thin SiO_2 layers, our method also provides sensitivity to the interface conductance between SiO_2 and Si and we find $G_{Si} = 0.6$ GW m^{-2} K^{-1} as the lower limit.

DOI: 10.1103/PhysRevB.95.184305

I. INTRODUCTION

Thermal transport across interfaces plays a key role in the thermal management and engineering of nanocomposites, nanoelectronics, and the next generation of magnetic data storage [1,2]. However, the challenges associated with measuring heat flows and temperature have hampered the field of thermal science at the nanoscale from achieving the same level of understanding and control as exists in electronics and photonics [3,4].

The interface thermal conductance G is a linear transport coefficient that describes the heat flux J crossing an interface for a given temperature difference ΔT between the distributions of heat carriers incident on the two sides of the interface, $J = G\Delta T$ [5]. G has been studied for interfaces between metals and dielectrics or metallic crystals and for metal-liquid interfaces [3,6]. For interfaces between crystals, the value of G is typically discussed in the context of scattering of well-defined phononic or electronic modes at the interface governed by interfacial bonding, disorder, and differences in the elastic constants or densities of states [7]. For interfaces with liquids, G is usually explained by molecular interactions at the interface and the overlap of densities of states.

In amorphous materials, only phonons near the zone center have well-defined wave vectors and the majority of the vibrational states that are important for heat transport lack coherence. The conduction of heat in an amorphous material can be described by a random walk of vibrational energy [8,9]. This fundamental difference in the heat carriers in amorphous and crystalline materials raises the question if conventional models for the interfacial thermal conductance can be applied reliably to boundaries with amorphous materials. Due to limited experimental accessibility, thermal transport at a boundary between a metal and an amorphous dielectric has not received much attention.

Well-established methods for studying thermal properties of interfaces are time-domain thermoreflectance (TDTR) [3,10] and frequency-domain thermoreflectance (FDTR) [11,12]. They are pump-probe techniques that measure the temperature response of a metal transducer to pulsed laser heating. Changes in the intensity of reflected laser probe pulses contain information about the thermal properties of the sample underneath the transducer. The sensitivity of a TDTR measurement to the interface conductance depends on the thermal mass (product of thickness h and volumetric heat capacity C) of the transducer. To separate the conductance G of an interface from the bulk thermal conductivity Λ of a sample underneath the transducer, h should not be large compared to the Kapitza length $L_K = \Lambda/G$. For SiO_2 and a typical conductance value of $G = 150$ MW m^{-2} K^{-1}, this means a transducer should not be significantly thicker than 10 nm. However, TDTR and FDTR require optically opaque transducers to avoid spurious thermoreflectance signals generated by the temperature field and changes in optical constants in the sample under the transducer [13]. In most cases, the requirement of an optically opaque metal-film transducer limits the transducer thickness to $h > 50$ nm and the sensitivity of TDTR or FDTR to the conductance G of interfaces with low thermal conductivity materials is typically small, on the order of $\frac{\Lambda}{hG}$.

Nevertheless, there are a few prior reports of conductance values for metal/SiO_2 interfaces measured by TDTR or FDTR. O'Brien *et al.* [14] studied bonding-induced thermal conductance enhancement for Cu/SiO_2 interfaces using TDTR and Cu transducers with thicknesses between 38 and 98 nm. They report a conductance value of $G_{Cu} = 90 \pm 15$ MW m^{-2} K^{-1} for untreated interfaces, and an up to fivefold enhancement of the conductance after chemical functionalization. For Al/SiO_2 interfaces conductance values reported range from 100 to 150 MW m^{-2} K^{-1} measured with 100-nm-thick Al transducers [12,15]. In the later publications no systematic uncertainties are given. All these experiments do not provide sufficient sensitivity to quantify G with low uncertainties. Reason for this is that the thermal mass of an optically thick transducer in combination with the low thermal conductivity

*jkimling@illinois.edu

†Present address: Deutsches Elektronen-Synchrotron (DESY), Notkestraße 85, 22607 Hamburg, Germany.

of amorphous SiO_2 samples results in a negligible temperature drop across the interface. At low frequencies or for thin SiO_2 layers on Si, the effective thermal conductivity of the sample is reduced. This results in an increase of the sensitivity with respect to G. However, as uncertainties add in quadrature and additional sample parameters (thickness of the oxide layer, conductance of the SiO_2/Si interface, and thermal conductivity of Si) have to be considered, the effective uncertainty does not actually decrease.

To gain better sensitivity than provided by conventional TDTR experiments, we replace the optically thick metal-transducer layer by a magnetic thin film with greatly reduced thermal mass. Instead of thermoreflectance, we rely on the transient polar Kerr rotation to selectively probe the temperature of the magnetic transducer and avoid artifacts created by the temperature distribution in the sample underneath.

In an earlier publication, we used a 20-nm-thick Co/Pt multilayer transducer on 300-nm-thick SiO_2 on Si and reported the value $G_{Pt} = 180 \pm 20$ MW m^{-2} K^{-1} [16]. In this study, both G and Λ were treated as free parameters and adjusted simultaneously. This approach led to an underestimation of the error in G due to the dominance of the sensitivity to Λ. Assuming 5% uncertainty in the heat capacity of the transducer film and 5% uncertainty in the thermal conductivity of the oxide, the results should read $G_{Pt} = 180 \pm 100$ MW m^{-2} K^{-1}. Here, we refine this approach by using Co/Pt transducers as thin as 4.2 nm and determine the conductance G_{Pt} between Pt and SiO_2 with a significantly reduced uncertainty.

In principle, our time-resolved magneto-optic Kerr-effect (TR-MOKE) method also provides access to the conductance G_{Si} of SiO_2/Si interfaces for which similar sensitivity considerations apply as for metal/SiO_2 interfaces. G_{Si} values reported to date vary by orders of magnitude. For example, values of 12–20 MW m^{-2} K^{-1} were measured by TDTR and FDTR using 100-nm-thick Al transducers [12,15], while Hurley *et al.* estimate a conductance of 0.4 GW m^{-2} K^{-1} based on time-resolved thermal wave microscopy [17]. Thus, we also measure the conductance G_{Si} of the SiO_2/Si interface on a sample with a 26-nm-thin SiO_2 layer on Si.

Sections II A and II B provide information about the samples and our experimental setup. Thermal modeling and data analysis are presented in Sec. II C. A detailed discussion of sensitivities of TDTR and TR-MOKE experiments is given in Sec. II D. Section III presents our experimental results including reference measurements on sapphire.

II. METHOD

A. Sample details

Amorphous SiO_2 films with thicknesses of 26 and 440 nm were grown on p-type Si ⟨001⟩ wafers in a furnace at 1000 °C in ambient atmosphere. SiO_2 thicknesses were measured by ellipsometry.

Co/Pt thin-film transducers with total thicknesses of 4.2, 5.5, and 8.2 nm were deposited at room temperature at a base pressure below 2×10^{-9} mbar: Pt seed layers with thicknesses between 0.8 and 3.5 nm were grown via ion-beam sputtering utilizing an electron cyclotron resonance (ECR) source. Subsequently, *in situ* dc magnetron sputtering was employed to deposit approximately 1 nm of Pt, a 0.7-nm-thick Co layer, and a between 1.7- and 3-nm thick Pt capping layer to prevent oxidation [18,19]. For reference measurements a sapphire (0001) substrate was added to the deposition of 4.2 nm Co/Pt. Furthermore, a sapphire (0001) substrate was coated with 43 nm of Pt by ECR sputtering for TDTR.

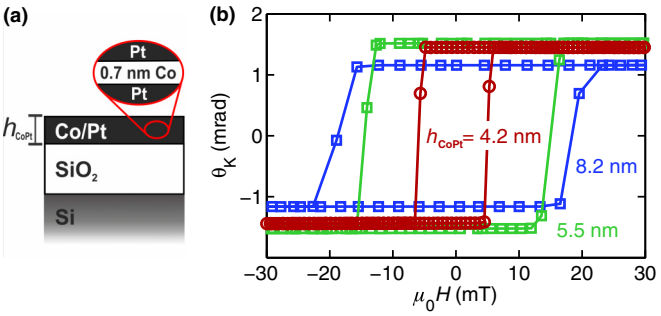

FIG. 1. (a) Schematic of Co/Pt transducer films on SiO_2/Si samples. (b) Hysteresis of Co/Pt thin films with total thicknesses of 4.2 nm (red), 5.5 nm (green), and 8.2 nm (blue) on 440-nm SiO_2 measured by polar magneto-optic Kerr effect at a wavelength of $\lambda = 635$ nm. The magnetic field was applied along the easy axis perpendicular to the sample plane.

Co/Pt and Pt film thicknesses were determined by x-ray reflectivity. Some samples were also characterized by Rutherford backscattering spectrometry to confirm thicknesses and composition. Details for individual samples are listed in Tables II and III in the Appendix. Figure 1(a) depicts a schematic of our samples. Pt forms a smooth interface with the underlying SiO_2 substrate. The roughness is approximately 0.2 nm, so on the order of one monolayer, the intermixing region is approximately 0.4 nm [19]. All Co/Pt films have perpendicular magnetic anisotropy, a remanence of one, and coercive fields between 6 and 18 mT [compare Fig. 1(b)].

B. Setup

We use an experimental setup with two detection schemes for TDTR and TR-MOKE measurements (see Fig. 2). The laser emits pulses with a full width at half-maximum (FWHM) spectral width of approximately 10 nm centered at 783 nm. Duration of correlated pump and probe pulses is approximately 1.2 ps. Pump and probe beams are split by a polarizing beam splitter (PBS) and separated spectrally using ultrasteep edge filters, namely, a long-pass filter in the pump path and short-pass filters in the probe path [20]. The pump beam is modulated at a frequency f of approximately 11 MHz by an electro-optic modulator (EOM) and the probe beam is modulated at 200 Hz by a mechanical chopper to suppress background signals at 10 MHz, e.g., signals originating from coherent pickup. Time delay between pump and probe pulses is varied from −25 ps to 3.6 ns using a mechanical delay stage. Both beams are focused on the sample by an objective lens to a $1/e^2$ radius of 11 μm. We use low fluences of approximately 0.07 J m^{-2} for both pump and probe beam, resulting in transient per-pulse heating on the order of 10 K. The reflected beams are split by a nonpolarizing beam splitter (BS) to detect both TDTR and TR-MOKE signals. For TDTR detection, the reflected pump light is removed by a PBS and

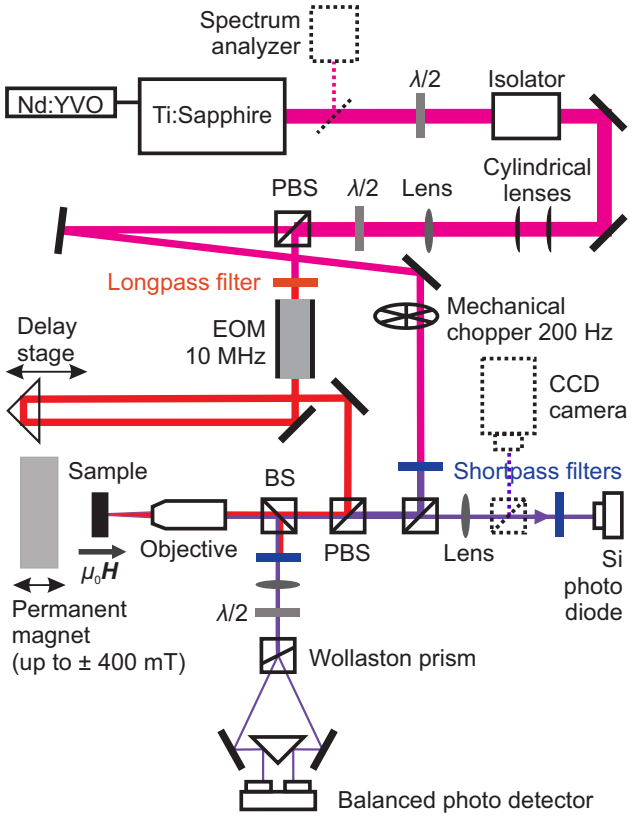

FIG. 2. Experimental setup. Pump and probe beam paths are split by polarizing beam splitters (PBS) and spectrally using short-pass (blue) and long-pass (orange) filters. Time-domain thermoreflectance (TDTR) is measured with a Si photodiode. Part of the beams reflected from the sample is redirected by a beam splitter (BS) towards a balanced photodetector to measure the time-dependent changes in Kerr rotation (TR-MOKE).

a short-pass filter identical to the one in the probe path. The probe beam is focused on a Si photo diode (PD). A low-pass filter removes higher harmonics before the output of the PD is measured by a radio-frequency lock-in amplifier at 11 MHz and subsequently by an audio-frequency lock-in amplifier at 200 Hz. For TR-MOKE detection the reflected pump light is blocked by an ultrasteep edge short-pass filter before the probe beam passes through a $\lambda/2$ plate and is split into orthogonally polarized components by a Wollaston prism. The $\lambda/2$ plate is adjusted such that both beam components focused onto a balanced photodetector (BPD) have approximately the same intensity. Transient changes in the polarization of the probe beam are proportional to changes in the relative intensities detected by the BPD. The radio-frequency output of the BPD is measured the same way as TDTR using a band-pass filter after the BPD.

In case of nonperfect balancing with the $\lambda/2$ plate, thermoreflectance signals overlap the transient Kerr rotation. To isolate the TR-MOKE signal we subtract the in-phase and out-of-phase signals recorded for oppositely aligned magnetization states of the Co/Pt transducers before analyzing the ratio signal $-V_{\text{in}}/V_{\text{out}} = -(V_{\text{in}}^{+} - V_{\text{in}}^{-})/(V_{\text{out}}^{+} - V_{\text{out}}^{-})$ as illustrated in Ref. [16]. Given the magnetic properties of our samples (compare Fig. 1) the magnetic field of approximately 400 mT provided by a NdFeB permanent magnet is sufficient to invert the direction of the magnetization of the Co/Pt transducer. Our "triple-modulation" approach (in addition to modulating pump and probe beam we modulate the magnetic state of the sample) makes TR-MOKE thermometry less prone to error as it ensures getting rid of offsets which can significantly affect TDTR experiments.

All measurements were done at remanence and room temperature.

C. Thermal model and data analysis

We analyze the ratio $R_{\text{data}} = -V_{\text{in}}/V_{\text{out}}$ using a multilayer heat diffusion model [21]. Analyzing the ratio instead of V_{in} alone corrects for nonidealities in the experiment such as laser power fluctuations and variations in pump-probe overlap with delay time [22]. A thermal model is fitted to the data in the delay-time range of highest sensitivity with respect to the interface thermal conductance [30–500 ps for G_{Pt}, compare Fig. 4(b)] by minimizing the sum of variances $\sigma = \sum[(R_{\text{model}} - R_{\text{data}})/R_{\text{data}}]^2$.

Table I summarizes all parameters including assumptions about the uncertainties that are used as inputs to the thermal model. Each layer of the sample is described by three parameters: thermal conductivity Λ, volumetric heat capacity C, and thickness h. Interfaces are modeled by layers with small heat capacity and thickness.

Given the small thermal masses of our Co/Pt transducers, adsorbates on the sample surface can notably add to the effective heat capacity of the transducer and have to be considered in our thermal model. Under normal environmental conditions as they were present during our experiment, hydrocarbons and water get adsorbed on the surface of solids [23]. The thickness of the water layer is known to be in the nanometer range and depends on the humidity of the ambient air and the conditions of the surface as oxidation state and carbonaceous contamination [24,25].

We empirically define C_{ad} as the heat capacity of adsorbed water and hydrocarbons, and accordingly add a transparent layer on top of the Co/Pt transducer. It does not matter how exactly we model this layer, as our thermal model only depends on the total heat capacity per unit area. We assign it a thickness of 1 nm and adjust the volumetric heat capacity.

C_{ad} is estimated by simultaneously fitting the volumetric heat capacity of this layer and the conductance G_{Pt} between Co/Pt transducer and SiO_2. Figure 3 shows contour plots obtained for 8.2 nm (blue), 5.5 nm (green), and 4.2 nm (red)

TABLE I. Parameters for model calculations and fitting of experimental data. h: layer thickness, Λ: thermal conductivity, C: volumetric heat capacity. Co/Pt films are treated as one layer.

	h (10^{-9} m)	Λ (W m^{-1} K^{-1})	C (10^{6} J m^{-3} K^{-1})
Adsorbate	1	2	2.8 ± 0.6
Co/Pt	$4.2/5.5/8.2 \pm 5\%$	20	2.97/2.94/2.90
SiO_2	$26 \pm 1/440 \pm 10$	1.31 ± 0.06	1.65
Si	∞	130 ± 7	1.61
Pt	43 ± 3	32	2.82
Al_2O_3	∞	35.5 ± 2	3.1

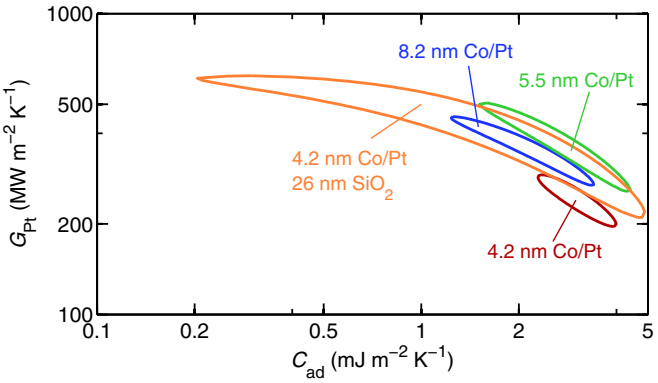

FIG. 3. Contour intervals marking the best agreement between TR-MOKE data and thermal model simultaneously adjusting conductance G_{Pt} between transducer and sample and heat capacity C_{ad} of adsorbates. For the 4.2-nm Co/Pt film on 26-nm SiO_2/Si (orange) the contour is much wider compared to the Co/Pt films on 440-nm-thick oxide (others). The reason for this is the increased noise in the data arising from the smaller out-of-phase signal due to the higher thermal conductivity of the substrate.

Co/Pt on 440-nm SiO_2, as well as 4.2-nm Co/Pt on 26-nm SiO_2 (orange). Lines include all combinations of the free parameters G_{Pt} and C_{ad} for which $\sigma \leqslant 2\sigma_{\mathrm{min}}$, where σ_{min} is the minimum of the sums of variances.

Considering the centers of the contours which mark the best fits, we find an average of $C_{\mathrm{ad}} = 2.8$ mJ m^{-2} K^{-1} and use this value for the analysis of all Co/Pt and Pt samples. The standard deviation in the best-fit values is only 15%. However, we assume an uncertainty of 20% in C_{ad} to account for the uncertainty due to noise in the data which is reflected in the width of the contours.

The approach of considering an additional heat capacity to account for surface properties is not uncommon. Using Al transducers requires the addition of a heat capacity of $C_{\mathrm{Al}} = 7.3$ mJ m^{-2} K^{-1} to obtain the right answer in TDTR experiments. The smaller value $C_{\mathrm{ad}} = 2.8$ mJ m^{-2} K^{-1} we find for Pt seems reasonable considering the different nature of the additional heat capacities. Al oxidizes, while Pt is comparably inert and we do not expect oxidation given our experimental conditions. Differences in surface oxidation lead to different degrees of contamination with hydrocarbons and water. Heating our samples to 100 °C in a vacuum of 4×10^{-4} mbar did not significantly alter C_{ad}. The inevitable presence of carbonaceous contamination leads to a certain degree of chemisorption of water that is hard to remove [23]. Gradual chemisorption would also explain why we do not see a significant increase of C_{ad} after six months, independent of how the samples were stored (N_2 atmosphere or ambient conditions). Mass gain by carbonaceous contamination is diffusion limited and does not saturate [24]. This is the reason for the mass increase of kg-mass standards over the course of years, and in analogy an eventual increase in C_{ad} has to be expected.

Volumetric heat capacities of Co/Pt layers are calculated based on composition assuming $C_{\mathrm{Co}} = 3.73 \times 10^6$ J m^{-3} K^{-1} and $C_{\mathrm{Pt}} = 2.82 \times 10^6$ J m^{-3} K^{-1}. For the cross-plane thermal conductivity of Co/Pt we assume an approximate value of 20 W m^{-1} K^{-1} which is not of relevance for the results reported here. For the 43-nm-thick Pt film we determine an in-plane electronic contribution of 25 W m^{-1} K^{-1} from sheet resistance measurements using the Wiedemann-Franz law and add 7 W m^{-1} K^{-1} to account for the theoretical contribution from the lattice [26].

In our thermal model, heat is deposited in the center of the Co/Pt transducer layer (or at a depth of 11 nm in the 43 nm thick Pt film on Al_2O_3) to account for the fact that heat is deposited throughout the penetration depth of the laser light, and then spreads bidirectionally, down into the SiO_2/Si (Al_2O_3) substrate and up into the top layer that represents adsorbates.

Our thermal model does not require quantitative knowledge of the optical absorption in a sample. However, we model the absorption in our samples to estimate temperature excursions in our experiments. Furthermore, understanding how the thicknesses of the Co/Pt and SiO_2 layers determine absorption A, reflectance R, and magneto-optic Kerr rotation θ_{K} helps to optimize the sample design (see Appendix, Sec. B for details). The laser power was selected such that the average heating of the transducer by a single optical pulse is between 10 and 18 K. As all our Co/Pt transducers are not opaque, part of the laser light is absorbed in the Si substrates. However, the optical penetration depth in Si is large, and even if the entire laser power was absorbed by the Si substrate the temperature rise would be below 0.1 K and can thus be neglected in the thermal modeling.

We measured the static Kerr rotation θ_{K} between room temperature and 100 °C to confirm that the change in Kerr rotation is, to a good approximation, proportional to the change in temperature. Knowing the temperature excursion by a pump optical pulse we can also determine the temperature dependence of the magneto-optic Kerr rotation from the in-phase signal of a TR-MOKE measurement. For the 4.2-nm Co/Pt on 440-nm SiO_2 sample we find a constant value of $d\theta_{\mathrm{K}}/dT = -1.2 \pm 0.2 \times 10^{-5}$ rad K^{-1} at 30 °C, 70 °C, and 100 °C and conclude that the linearity of the TR-MOKE signal required for thermometry is given for the transducers under investigation. Table III summarizes the averaged $d\theta_{\mathrm{K}}/dT$ and θ_{K} values at room temperature for all samples studied. $d\theta_{\mathrm{K}}/dT$ is, to a good approximation, proportional to θ_{K}. We find an average ratio of $\frac{\theta_K}{d\theta_{\mathrm{K}}/dT} = 485 \pm 25$ K.

D. Sensitivities in TDTR and TR-MOKE thermometry

The thermal penetration depth $d = \sqrt{\frac{\Lambda}{C\pi f}}$ in a material with volumetric heat capacity C and thermal conductivity Λ is determined by the modulation frequency f of the EOM. We refer to a sample as "thermally thick" if its thickness is larger than d. For amorphous SiO_2, $d \approx 270$ nm at $f = 11$ MHz. This means that the thermal conductance of the SiO_2/Si interface and the thermal conductivity of Si are not important in experiments using 440-nm-thick SiO_2.

To describe the sensitivity of the measurement signal to properties of the materials at depths shorter than the thermal penetration depth, we define sensitivity coefficients S_α as the

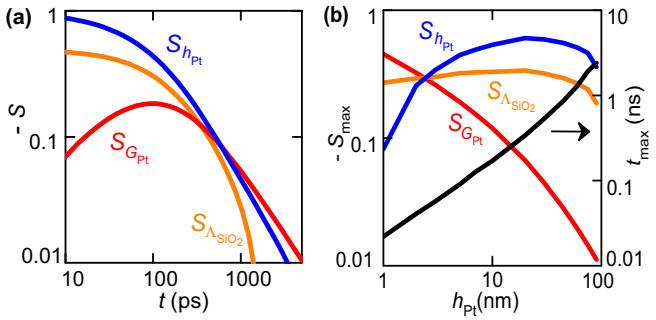

FIG. 4. (a) Sensitivity coefficients with respect to interface conductance G_{Pt} (red), transducer thickness h_{Pt} (blue), and thermal conductivity Λ_{SiO_2} (orange) versus delay time t for a 5-nm-thick Pt transducer on thermally thick oxide. Simulation parameters are listed in Table I, $G_{Pt} = 0.25$ GW m^{-2} K^{-1}. (b) Maximum sensitivity coefficients S_{max} at delay time of maximum sensitivity t_{max} calculated for various thicknesses h_{Pt}.

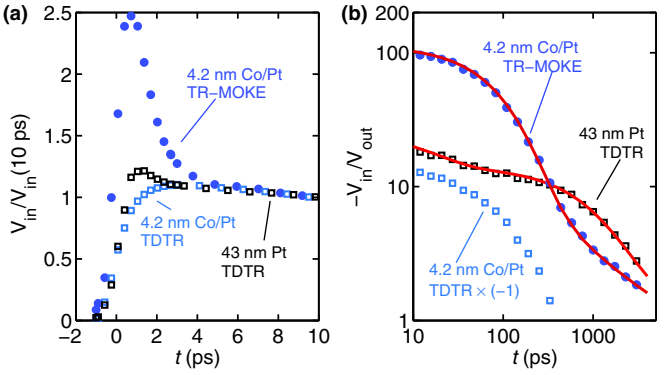

FIG. 5. Data measured by time-domain thermoreflectance (TDTR, open squares) with 4.2-nm Co/Pt (blue) and with 43-nm Pt (black) transducer, and by time-resolved magneto-optic Kerr effect (TR-MOKE, blue circles) with 4.2-nm Co/Pt transducer on Al_2O_3. (a) Normalized in-phase signals. (b) Ratio signals, blue squares are multiplied by -1 as ratio is negative. Red lines are the best fits obtained using the interface conductance G between Pt and sapphire as only free parameter. Model parameters are listed in Table I. $C_{ad} = 2.8$ mJ m^{-2} K^{-1} was considered for both samples.

logarithmic derivative of the negative of the ratio signal:

$$S_\alpha = \frac{\partial[\ln(-V_{in}/V_{out})]}{\partial[\ln(\alpha)]}, \quad (1)$$

where α is a parameter in the thermal model [27].

Figure 4(a) depicts the delay-time dependence of S with respect to the transducer thickness h_{Pt} (blue), the conductance $G_{Pt} = 0.25$ GW m^{-2} K^{-1} (red), as well as the thermal conductivity Λ_{SiO_2} (orange) for a 5-nm-thin Pt transducer on thermally thick SiO_2. As in a conventional TDTR measurement, the sensitivities of the ratio signal to the thickness ($S_{h_{Pt}}$) and to the volumetric heat capacity ($S_{C_{Pt}}$, not shown, identical to $S_{h_{Pt}}$) of the transducer are large, close to unity at short delay times.

Figure 4(b) illustrates how the sensitivities with respect to G_{Pt}, h_{Pt}, and Λ_{SiO_2} depend on the thickness h_{Pt} of the transducer film. As S changes with delay time between pump and probe pulses, we plot the peak sensitivities S_{max} versus h_{Pt}. The black line indicates the delay times t_{max} at which the sensitivity to the conductance G_{Pt} reaches the maximum value S_{max}.

A characteristic time scale for the measurement is the time required for heat to diffuse a distance in SiO_2 that is equal to the Kapitza length, $\tau_D = L_K^2 C_{SiO_2}/\Lambda_{SiO_2}$. The sensitivity to G_{Pt} is at a maximum for delay times comparable to τ_D although the exact position of the maximum is also a function of h_{Pt} relative to L_K.

For a typical, 90-nm optically thick Pt transducer, the peak sensitivity to G_{Pt} is $S_{max} \approx -0.01$ and occurs at a delay time of $t_{max} = 2$ ns. This means a 100% variation in G would change the ratio signal $-V_{in}(t_{max})/V_{out}(t_{max})$ by 1%. Reduction of the transducer thickness leads to a significant increase in S_{max}, as the temperature change and thus the signal change for a given amount of heat diffusion across the Pt/SiO_2 interface is bigger the smaller the thermal mass of the transducer. To gain reasonable sensitivity of $|S| \geqslant 0.1$, the transducer thickness has to be on the order of the Kapitza length $L_K = \Lambda_{SiO_2}/G_{Pt}$ in SiO_2, which is approximately 5 nm for a conductance of $G_{Pt} = 250$ MW m^{-2} K^{-1}.

An uncertainty u_α in a model parameter α propagates into the uncertainty u_β of a free parameter β according to $u_\beta = u_\alpha \frac{S_\alpha}{S_\beta}$. Uncertainties arising from different model parameters add in quadrature. The experimental uncertainty in G_{Pt} based on 5% uncertainty in both h_{Pt} and Λ_{SiO_2} is 80% using a 90-nm-thick transducer film, 12% for a 10-nm transducer, and 6% for a 5-nm-thin transducer. Here, we only considered the S_{max} values. For the analysis of our data we consider the maximum of each sensitivity coefficient within the entire fitted time range as well as additional sources of uncertainty as the heat capacity of water and hydrocarbons adsorbed on the surface of the sample.

III. RESULTS AND DISCUSSION

A. Comparison of TDTR and TR-MOKE data for sapphire samples

To test our experimental approach, we compare TDTR and TR-MOKE measurements done with a 4.2-nm-thin Co/Pt film on sapphire, as well as a reference TDTR measurement using a 43-nm-thick Pt film on the same Al_2O_3 substrate. Figure 5(a) displays normalized in-phase signals for short time delays t between pump and probe laser pulses. The difference in TDTR traces (open squares) arises from the fact that the electronic contribution to the thermoreflectance, which leads to a small peak in the Pt data (black) at delay times around 1 ps, is negligible for the 4.2-nm-thin Co/Pt transducer (blue).

TR-MOKE (full blue circles) probes the magnon temperature. We see the characteristic ultrafast demagnetization peak at ≈1 ps, which looks the same for all Co/Pt samples studied. Magnons, electrons, and phonons are thermalized at delay times >2 ps due to strong electron-magnon coupling, strong electron-phonon coupling, and the small heat capacity of the magnons at temperatures far away from the Curie point [28].

The time it takes for a transducer to reach equilibrium determines the shortest time delay at which our thermal model can be fitted to the experimental data. In TR-MOKE experiments using ultrathin magnetic films as transducers it can be

limited by either the thermalization times between the thermal reservoirs or by the time it takes to establish a homogeneous temperature distribution across the thickness of the transducer. Close to the Curie temperature T_C, the magnetic heat capacity increases. This slows down the demagnetization process and can lead to thermalization times of up to 100 ps [28]. Due to the magnetic properties of Co/Pt films and the small transient heating by our laser pulses (≈10 K), our experiments are conducted well below T_C.

Red lines in Fig. 5(b) are the fits obtained adjusting the interfacial thermal conductance G between Pt and Al_2O_3 as only free parameter in our thermal model. The results are in agreement within the uncertainty of our measurements. We find $G = 170 \pm 10$ MW m^{-2} K^{-1} analyzing TR-MOKE data for 4.2-nm Co/Pt (blue circles) and $G = 145 \pm 15$ MW m^{-2} K^{-1} analyzing TDTR data for 43-nm Pt (black squares). The shortest delay times fitted are 10 and 100 ps, respectively. For both samples, an adsorbed layer with $C_{ad} = 2.8 \pm 0.6$ mJ m^{-2} K^{-1} was considered in the thermal modeling.

TR-MOKE selectively probes the magnon temperature of a ferromagnetic transducer layer. TDTR, on the other hand, probes the phonon and electron temperatures of all regions within the penetration depth of the laser light. Even in case of a transparent sample as Al_2O_3, which does not contribute much to the thermoreflectance signal, an opaque transducer is essential in TDTR experiments. To demonstrate this, we also plot the TDTR ratio signal measured with the 4.2-nm-thin Co/Pt film [see blue squares in Fig. 5(b)]. The ratio is negative which is not possible if the thermoreflectance signal is dominated by the changes in the temperature of the Co/Pt film. On SiO_2/Si substrates we find that a Pt thickness of 50 nm (corresponding to approximately five times the optical penetration depth) is required to guarantee that TDTR and TR-MOKE ratios are identical after equilibration of the transducer (data not shown).

B. Thermal conductance of Pt/*a*-SiO_2 interfaces

Thermal conductance G_{Pt} of Pt/*a*-SiO_2 interfaces was measured on four different samples with thin Co/Pt transducers. TR-MOKE data and fit curves are presented in Fig. 6(a) for 4.2-, 5.5-, and 8.2-nm Co/Pt on 440-nm SiO_2, as well as in Fig. 8 for 4.2-nm Co/Pt on 26-nm SiO_2. Considering the sensitivity each sample provides with respect to G_{Pt} we find an average value of $G_{Pt} = 310 \pm 50$ MW m^{-2} K^{-1}. Here, the error originates from the scattering of best-fit results for the individual samples and does not represent an experimental uncertainty based on model parameters which is larger [compare Fig. 6(b)].

Figure 6(b) summarizes our results and compares them to the work of Liu *et al.* which provided the highest sensitivity to a comparable interface prior to this work. Experimental advancement through using transducers of greatly reduced thermal mass is reflected in the width of error bars. By using 4.2-nm-thin transducers, the uncertainty can be reduced down to approximately 20%, compared to 60% uncertainty when using 20-nm-thick Co/Pt films. Note that the advancement is masked by the fact that values for S with respect to G_{Pt} as well as to other experimental parameters (most critically Λ_{SiO_2}) depend on the absolute conductance values measured.

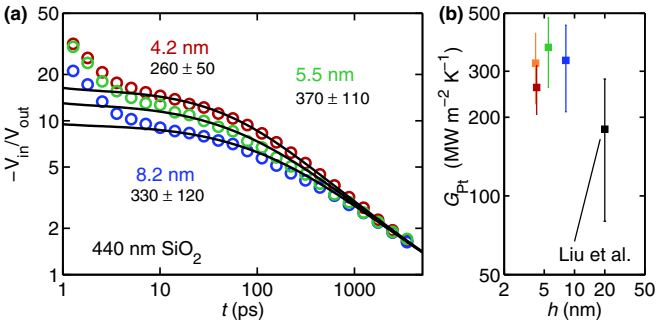

FIG. 6. (a) TR-MOKE ratio data versus delay time t measured using Co/Pt transducers with thicknesses of 4.2 nm (red), 5.5 nm (green), and 8.2 nm (blue) on 440-nm (thermally thick) SiO_2. Black lines are fits of thermal models to the data obtained treating G_{Pt} as only free parameter and considering an adsorbed layer with a heat capacity of $C_{ad} = 2.8$ mJ m^{-2} K^{-1}. Black numbers are conductances in MW m^{-2} K^{-1}. (b) Results for conductances from this work [orange point for 4.2-nm Co/Pt on 26-nm SiO_2, other color coding as in panel (a)] and data by Liu *et al.* [16]. All error bars are calculated assuming same relative uncertainty in experimental parameters.

The higher the interface conductance, the more difficult it is to separate its contribution from the conductivity of the SiO_2.

The values we measure for the interface conductance G_{Pt} between metal and an amorphous material are higher than the ones reported for comparable interfaces to date [12,14,16]. As shown both experimentally and in molecular dynamics simulations, conductance can be significantly increased by enhancing interfacial bonding [14,29,30]. Bonding at the interface between a metal and *a*–SiO_2 can be weakened by layers of contamination adsorbed on the oxide surface. Based on the results of earlier studies [18,19], we believe that the Pt/SiO_2 interface is relatively free of such contamination layers because we use the electron-cyclotron resonance (ECR) sputtering technique to deposit the first part of the Pt seed layer on SiO_2 (followed by an additional 1-nm Pt by magnetron sputtering). During ECR sputter deposition high-energy Ar^+ ions ($\leqslant$1.2 keV) reflected at the target bombard the surface of the SiO_2 substrate and remove contamination. Pt atoms impinge the surface with kinetic energies of ≈ 30 eV [19]. This enhances bonding and potentially drives some degree of intermixing of atoms at the interface [18].

Since in a metal heat is mainly carried by electrons and in amorphous SiO_2 it is carried only by vibrational modes, the effective conductance can be considered as the series of two thermal resistances. The conductance value G_{Pt} we measure is thus given by $G_{Pt} = 1/(G_{el\text{-}ph}^{-1} + G_{vib}^{-1})$. Assuming a coupling constant of $g = 4.2 \times 10^{17}$ W m^{-3} K^{-1} [31], $G_{el\text{-}ph} = g\,h$ yields approximately 2 GW m^{-2} K^{-1} and higher for our samples. The vibrational energy transfer across the interface is thus the main source of thermal resistance.

For a crystalline material, the corresponding conductance G_{vib} is given by $G_{vib} = \frac{1}{4}\sum_j \int t_\omega v_\omega c_\omega d\omega_j$ [5,32] where v_ω are the group velocities and c_ω are the heat capacities of phonons with frequency ω_j and polarization j. $c_\omega = \hbar\omega D_\omega \partial n_\omega/\partial T$, where D_ω is the density of states, n is the Bose-Einstein distribution function. We define a maximum conductance value G_{max} for a material by setting the

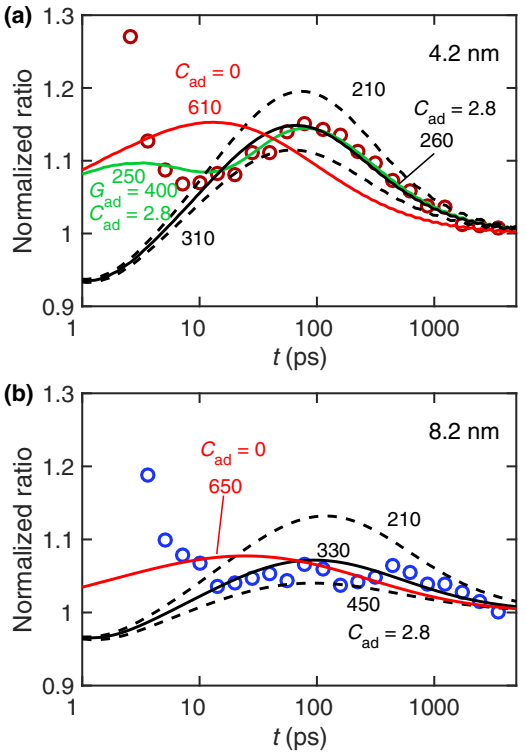

FIG. 7. TR-MOKE ratios normalized by models for $C_{ad} = 0$ mJ m^{-2} K^{-1}, no Pt/SiO$_2$ interface, and no adjusted parameters to highlight deviations between data and model curves. Data points and black curves are same as in Fig. 6(a). Dashed lines are models representing experimental uncertainties. Red lines are best fits obtained not considering the additional heat capacity of adsorbates. C_{ad} values are in mJ m^{-2} K^{-1}, numbers next to model lines are conductance values G_{Pt} in MW m^{-2} K^{-1}. Green model line in (a) includes an interface with conductance $G_{ad} = 400$ MW m^{-2} K^{-1} between Co/Pt transducer and adsorbed layer.

transmission coefficient $t = 1$. G_{max} for an interface is determined by the material that has the lower intrinsic G_{max} value. Following the calculation described in Ref. [32], we obtain a theoretical value of $G_{max} = 0.9$ GW m^{-2} K^{-1} for Pt. For interfaces between metals and dielectric crystals, the experimental values for G typically lie around $G_{max}/3$, and up to $G_{max}/2$ for strongly bonded interfaces. The values we measure fall into this range.

C. Thermal model and the role of adsorbates

To better see deviations between model curves and experimental data, we plot the data for 4.2- and 8.2-nm Co/Pt shown in Fig. 6(a) again in Figs. 7(a) and 7(b), normalizing all curves to models with the thermal resistance of the Pt/SiO$_2$ interface and the additional heat capacity C_{ad} due to adsorbates set to zero. All model parameters are listed in Table I. As discussed in Sec. II C, we use contour plots (compare Fig. 3) to estimate the heat capacity of adsorbed hydrocarbons and water and add the averaged value of $C_{ad} = 2.8 \pm 0.6$ mJ m^{-2} K^{-1} to the thermal model for all samples. Black lines in Fig. 7 are the same fit curves as in Fig. 6(a) obtained treating G_{Pt} as the only remaining free parameter. Dashed black lines are model curves

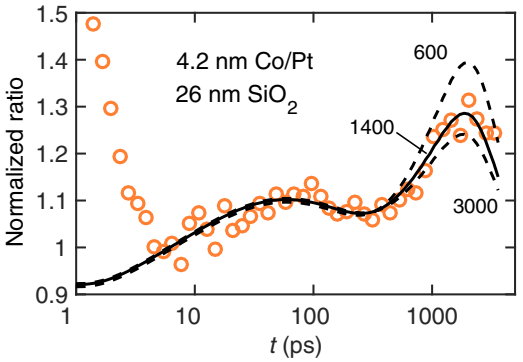

FIG. 8. TR-MOKE ratio data measured with 4.2-nm-thin Co/Pt transducers on 26-nm SiO$_2$. Thermal models include an adsorbed layer with a heat capacity of $C_{ad} = 2.8$ mJ m^{-2} K^{-1} added on top of the Co/Pt. Conductance $G_{Pt} = 320 \pm 110$ MW m^{-2} K^{-1} of the Pt/SiO$_2$ interface was fitted between 30 and 500 ps. Black numbers are conductances G_{Si} between SiO$_2$ and Si in MW m^{-2} K^{-1} fitted between 800 and 3600 ps. All curves are normalized by models for $C_{ad} = 0$ mJ m^{-2} K^{-1} and no Pt/SiO$_2$ and SiO$_2$/Si interfaces.

representing the error bars based on uncertainties in the model parameters.

For comparison, we also plot the best fits obtained neglecting the additional heat capacity due to an adsorbed layer and treating G_{Pt} as only free parameter (see red lines in Fig. 7). Not considering C_{ad} reduces the thermal masses of the transducers and thus remarkably increases the sensitivity to G_{Pt}, especially for the 4.2-nm sample. Consequently, we see a notable deviation of the normalized curves from one (representing the model for infinite conductance), even though the fitted conductance values are higher than 600 MW m^{-2} K^{-1}. The delay time of highest sensitivity to G_{Pt} is at approximately 20 ps, compared to 80–100 ps for the models including an adsorbed layer. Comparison to the curvature in our data clearly underlines the validity of our thermal model considering the additional heat capacity.

The green line in Fig. 7(a) is a model considering the interface between Co/Pt transducer and adsorbed layer as additional free parameter. Adjusting G_{Pt} and the conductance G_{ad} of this interface at delay times between 10 and 500 ps yields $G_{Pt} = 250$ MW m^{-2} K^{-1} and $G_{ad} = 400$ MW m^{-2} K^{-1}. Introducing this interface does not significantly change the result of our thermal analysis. However, the fit between model curve and data clearly improves at short delay times. This demonstrates that ultrathin Co/Pt transducers provide a platform for a more profound study of the thermal properties of adsorbed molecular layers and facilitate access to heat diffusion processes occurring at picosecond time scales.

D. Thermal conductance of a-SiO$_2$/Si interfaces

Our TR-MOKE method also gives access to the conductance G_{Si} between a-SiO$_2$ and Si for a carefully chosen thickness of the oxide layer that provides a separation of the delay times at which maximum sensitivities to G_{Pt} and G_{Si} occur.

We characterized a sample with 4.2-nm Co/Pt on 26-nm SiO$_2$/Si by TR-MOKE thermometry. Figure 8 depicts ratio

data and model curves normalized to models with the thermal resistances of the Pt/SiO_2 and SiO_2/Si interfaces and the additional heat capacity due to adsorbed hydrocarbons and water set to zero. We find $G_{Si} = 1.4$ GW m^{-2} K^{-1}. Because of the small sensitivity to such a high conductance value, the error bars are large, ± 1.6 GW m^{-2} K^{-1}. Since sensitivity coefficients scale with G_{Si}, symmetrical error bars do not reflect the physical reality. The dashed lines in Fig. 8 representing the uncertainties are thus drawn for $G_{Si} = 3$ GW m^{-2} K^{-1} and $G_{Si} = 0.6$ GW m^{-2} K^{-1}. Our lower limit for G_{Si} considers error propagation from all uncertainties by considering the "worst-case" combination of model parameters. This worst-case combination of those parameters was selected as follows: For each model parameter α an uncertainty is assumed (compare Table I) that sets the minimum and maximum values possible for α. Depending on the sign of the sensitivity coefficient S_α compared to the sign of $S_{G_{Si}}$, either the minimum or maximum value of α was used. Fitting a thermal model with those parameters to the experimental data results in the lowest value possible for G_{Si} within our uncertainties. Our result agrees well with the lower limit we calculate from data reported by Costescu *et al.* [22].

Costescu *et al.* measured the thermal conductivity of thin SiO_2 layers on Si by TDTR using 60-nm-thick TiN transducers [22]. In their experiments, oxide layers were thin enough for the TiN/SiO_2 and SiO_2/Si interfaces to notably reduce the effective thermal conductivity. From their room-temperature data on 6.5- and 11-nm-thin SiO_2 we determine a lower limit for the SiO_2/Si interface of 0.5 GW m^{-2} K^{-1} by assuming an infinite conductance for the first interface. Based on the data by Costescu *et al.*, it is unclear how the thermal resistance splits between the TiN/SiO_2 and SiO_2/Si interfaces. If we assign a value of 600 GW m^{-2} K^{-1} to the TiN/SiO_2 interface, we calculate $G_{Si} = 4$ GW m^{-2} K^{-1}. The agreement with our result supports the assumption that the conductance of SiO_2/Si interfaces is very high.

Molecular dynamics simulations also predict high conductances on the order of 1 GW m^{-2} K^{-1} [33]. According to Ref. [32], the theoretical value of G_{max} for Si is 0.8 GW m^{-2} K^{-1}. Our experimental result for G_{Si} suggests that the transmission coefficient for vibrational heat flow at a Si/SiO_2 interface is close to unity.

IV. CONCLUSION

Selectively probing the temperature of magnetic thin films via TR-MOKE facilitates the use of transducers with significantly reduced thermal mass. Using this thermometry method, sensitivity to the conductance of interfaces with low thermal conductivity materials can be increased by approximately one order of magnitude compared to TDTR. The 4.2- to 8.2-nm-thin Co/Pt transducers used in our study provide sufficient sensitivity to quantify the interface thermal conductance between Pt and amorphous SiO_2. We find an average value of $G_{Pt} \approx 0.3$ GW m^{-2} K^{-1}. For SiO_2/Si interfaces we find a lower limit of $G_{Si} = 0.6$ GW m^{-2} K^{-1}.

Perpendicularly magnetized Co/Pt thin films can be grown on almost any sample [19,34], do not require annealing, and are comparably inert. They are thus ideal transducers for the TR-MOKE thermometry method demonstrated here. A critical aspect to consider which will vary depending on the transducer material selected, is the additional heat capacity due to adsorbed water and hydrocarbons, as well as due to possible oxide formation. In our samples, adsorbates increase the heat capacity by up to 20%.

As discussed in detail in the Appendix, Sec. B, the optical absorption behavior and the Kerr rotation in our samples are a function of the magneto-optic constants and thicknesses of the transducer and the underlying sample structure. Ferromagnetic transducers have thus to be optimized depending on the sample requirements with respect to magneto-optic properties, sensitivities, and time resolution. In our case, a transducer thickness of approximately 4 nm minimizes the thermal mass while maintaining a large Kerr signal.

We anticipate that magnetic thin-film transducers will provide a platform for measurements of small heat capacities, for example, of adsorbed molecular layers, and make it possible to study thermal processes on the picosecond time scale. The time resolution in optical pump-probe experiments is typically limited by the time scale $\tau_D = \frac{h^2 C}{\Lambda}$ of heat diffusion through a transducer with thickness h. In TDTR experiments with opaque Al transducers, τ_D is on the order of 100 ps, while it is only approximately 4 ps for TR-MOKE thermometry with a 5-nm-thin Co/Pt transducer. Access to such short time scales might allow for the observation of nonequilibrium effects of heat carriers directly in the time domain [35].

ACKNOWLEDGMENTS

This work was partially funded by the Office of Naval Research, MURI Grant No. N00014-16-1-2436. Samples were characterized at the Frederick Seitz Materials Research Laboratory Central Research Facilities, University of Illinois. The authors thank Johannes Kimling for help with the magneto-optic modeling as well as R. B. Wilson for fruitful discussions.

APPENDIX

A. Sample details

Table I lists the sample parameters relevant to the thermal modeling of our TR-MOKE experiment. In Table II, we provide information about the magnetic properties of the Co/Pt transducer films measured by static MOKE at a wavelength of 635 nm. Anisotropy constants were determined from hard-axis hysteresis loops. Coercive fields were measured with the external magnetic field applied along the easy axis, perpendicularly to the sample plane. Table III summarizes additional information about the samples relevant to the optimization of sample design.

B. Optimization of sample design

In TDTR and TR-MOKE measurements, the ratio signal $R = -V_{in}/V_{out}$ at short delay times is approximately proportional to $\frac{\sqrt{\Lambda_S C_S}}{hC}$. $\sqrt{\Lambda_S C_S}$ is the effusivity of the sample within the penetration depth of the thermal wave and hC is the thermal mass of the transducer. As the latter is drastically reduced in our TR-MOKE experiments, the ratio signals are larger than the ratio signals measured in typical TDTR experiments. Noise

TABLE II. Magnetic properties of Co/Pt films on 440-nm SiO_2. h: total thickness of Co/Pt transducer, K_1: effective magnetic anisotropy constant, $\mu_0 H_C$: coercive field.

h (nm)	$h_{Pt}/h_{Co}/h_{Pt}$ (nm)	K_1 (kJ m^{-3})	$\mu_0 H_C$ (mT)
4.2	1.8/ 0.7/1.7	230 ± 20	6
5.5	2.8/ 0.7/2	380 ± 40	14
8.2	4.5/ 0.7/3	400 ± 20	19

in our experimental ratio data mainly originates from the out-of-phase signal. V_{out} is inversely proportional to the effusivity and is on the order of 1×10^{-6} V for our fluence setting. The noise level in our signal is on the order of 5×10^{-8} V.

To minimize the time of data acquisition, it is thus of interest to maximize the amplitude of the measurement signal. In TR-MOKE thermometry, the signal strength is proportional to the temperature rise ΔT in the transducer (given by the laser fluence as well as the absorption and thermal mass of the transducer), the reflectance R of the sample, and the temperature dependence of the Kerr rotation $d\theta_K/dT$ (the equivalent to the thermoreflectance coefficient in TDTR experiments). To guarantee linear response, the temperature rise has to be limited, so the signal cannot be increased significantly by increasing the laser fluence.

Absorption behavior and magneto-optic properties of our samples strongly depend on the thicknesses of the Co/Pt and SiO_2 layers. In what follows, we present model calculations to illustrate how R and θ_K can be optimized by adjusting sample parameters. Assuming constant base temperature and stable magnetic properties, $d\theta_K/dT$ is proportional to the static Kerr rotation θ_K.

We use a transfer-matrix model as described in Ref. [36] to calculate absorption A, reflectance R, and Kerr rotation θ_K for our Co/Pt samples. Results are summarized in Table III and Fig. 9.

For simplicity we neglect the sandwich structure here and model the Pt/Co/Pt stack as one layer. Optical constants were measured by ellipsometry. As the dependence of the optical constants on layer thickness is weak (below 3%), we use the following complex refractive indices for all samples: $n_{Co/Pt} = 3.0 + 5.45i$; $n_{SiO_2} = 1.45$; $n_{Si} = 3.7 + 0.007i$; $n_{Al_2O_3} = 1.76$. As discussed by Fiedler *et al.*, magneto-optic constants Q for thin Pt/Co/Pt sandwiches depend on the individual layer thicknesses and are fingerprints of

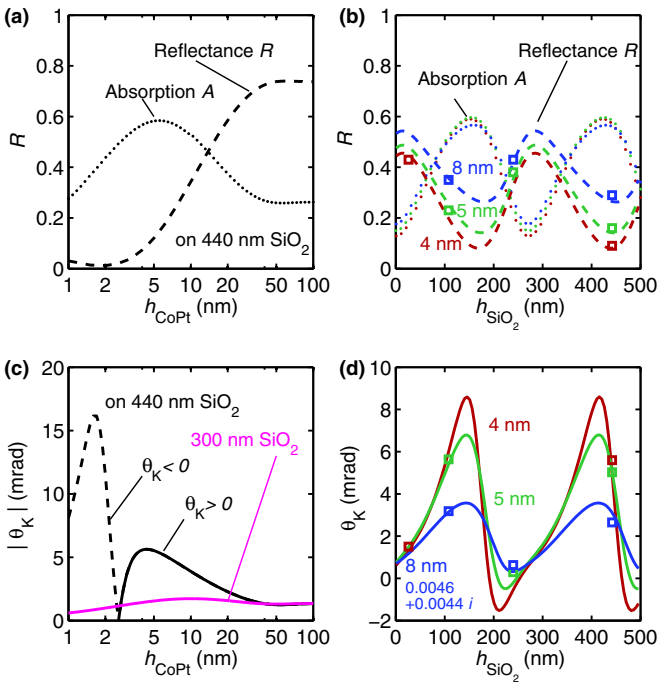

FIG. 9. Absorptions A (dotted) and reflectances R (dashed lines) calculated with a transfer-matrix model [36] for (a) Co/Pt transducers with varying thickness $h_{Co/Pt}$ on 440-nm SiO_2. (b) Models and measured reflectance values for $h_{Co/Pt} = 8.2$ nm (blue), 5.5 nm (green), and 4.2 nm (red) for varying SiO_2 thicknesses. (c) Kerr rotation angles θ_K versus $h_{Co/Pt}$ and (d) versus h_{SiO2} including experimental values. If not stated differently, $Q = 0.0063 - 0.062i$ was used as magneto-optic constant.

the complex structure of the magneto-optic active part of the film, probably determined also by intermixing at the Co/Pt interfaces [37]. They find $Q = 0.041 - 0.040i$ for a magnetron-sputtered Co layer. For our optical modeling we determine the effective magneto-optic constants for the entire layer by scaling Q to roughly adjust the model curves for θ_K to our experimental data [compare Fig. 9(d)]. We find good agreement using $Q = 0.0063 - 0.062i$ for the 4.2- and 5.5-nm-thin films, and $Q = 0.0046 - 0.044i$ for the 8.2-nm-thick film.

θ_K and thus $d\theta_K/dT$ can critically depend on the thickness of the transducer film [see Fig. 9(c)] and has a surprisingly strong dependence on the thickness of the underlying oxide

TABLE III. Sample parameters. h: total thickness of Co/Pt transducer, C: volumetric heat capacity, A: absorption, R: reflectance (calculated), R_{ex}: measured reflectance, θ_K: static Kerr rotation at room temperature and wavelength of 785 nm, $d\theta_K/dT$: temperature dependence of θ_K from TR-MOKE data.

Substrate	h (nm)	$h_{Pt}/h_{Co}/h_{Pt}$ (nm)	C (10^6 J m^{-3} K^{-1})	A	R	R_{ex}	θ_K (10^{-3} rad)	$d\theta_K/dT$ (10^{-5} rad K^{-1})
Al_2O_3	43	43/-/-	2.82	0.22	0.77	0.72		
Al_2O_3	4.2	1.8/0.7/1.7	2.97	0.29	0.26	-	2.5 ± 0.3	-0.5 ± 0.1
26-nm SiO_2/Si	4.2	1.8/0.7/1.7	2.97	0.18	0.45	0.43	1.4 ± 0.2	-0.3 ± 0.1
440-nm SiO_2/Si	4.2	1.8/0.7/1.7	2.97	0.58	0.08	0.09	5.6 ± 0.3	-1.2 ± 0.1
440-nm SiO_2/Si	5.5	2.8/0.7/2	2.94	0.59	0.15	0.16	5.2 ± 0.4	-1.1 ± 0.1
440-nm SiO_2/Si	8.2	4.5/0.7/3	2.9	0.56	0.27	0.29	2.6 ± 0.2	-0.5 ± 0.1

due to optical cavity effects [compare Fig. 9(d)]. On the quest for the ideal transducer material with high $d\theta_K/dT$, one should thus compare the magneto-optic constants rather than the actual Kerr rotation angles measured.

Optical cavity effects also lead to a strong wavelength dependence of A and θ_K, so static Kerr rotations presented in Fig. 1 (measured with laser wavelength $\lambda = 635$ nm) and Table III ($\lambda = 785$ nm) differ notably. The change in Kerr rotation due to the temperature rise in the SiO_2 is more than an order of magnitude smaller than $d\theta_K/dT$ based on the temperature change in the metal transducer itself for all samples studied, and thus negligible in our experiment.

[1] A. Shakouri, Proc. IEEE **94**, 1613 (2006).
[2] D. Weller and A. Moser, IEEE Trans. Magn. **35**, 4423 (1999).
[3] D. G. Cahill, P. V. Braun, G. Chen, D. R. Clarke, S. Fan, K. E. Goodson, P. Keblinski, W. P. King, G. D. Mahan, A. Majumdar *et al.*, Appl. Phys. Rev. **1**, 011305 (2014).
[4] M. D. Losego and D. G. Cahill, Nat. Mater. **12**, 382 (2013).
[5] R. J. Stoner and H. J. Maris, Phys. Rev. B **48**, 16373 (1993).
[6] D. G. Cahill, W. K. Ford, K. E. Goodson, G. D. Mahan, A. Majumdar, H. J. Maris, R. Merlin, and S. R. Phillpot, J. Appl. Phys. **93**, 793 (2003).
[7] R. Cheaito, J. T. Gaskins, M. E. Caplan, B. F. Donovan, B. M. Foley, A. Giri, J. C. Duda, C. J. Szwejkowski, C. Constantin, H. J. Brown-Shaklee *et al.*, Phys. Rev. B **91**, 035432 (2015).
[8] D. G. Cahill, S. K. Watson, and R. O. Pohl, Phys. Rev. B **46**, 6131 (1992).
[9] W. Lv and A. Henry, New J. Phys. **18**, 013028 (2016).
[10] P. E. Hopkins, ISRN Mech. Eng. **2013**, 682586 (2013).
[11] A. J. Schmidt, R. Cheaito, and M. Chiesa, Rev. Sci. Instrum. **80**, 094901 (2009).
[12] J. Zhu, D. Tang, W. Wang, J. Liu, K. W. Holub, and R. Yang, J. Appl. Phys. **108**, 094315 (2010).
[13] W. S. Capinski, H. J. Maris, T. Ruf, M. Cardona, K. Ploog, and D. S. Katzer, Phys. Rev. B **59**, 8105 (1999).
[14] P. J. O'Brien, S. Shenogin, J. Liu, P. K. Chow, D. P. Laurencin, P. Mutin, M. Yamaguchi, P. Keblinski, and G. Ramanath, Nat. Mater. **12**, 118 (2013).
[15] P. Hopkins, J. Serrano, L. Phinney, S. Kearney, T. Grasser, and C. Harris, ASME. J. Heat Transfer **132**, 081302 (2010).
[16] J. Liu, G.-M. Choi, and D. G. Cahill, J. Appl. Phys. **116**, 233107 (2014).
[17] D. H. Hurley, M. Khafizov, and S. L. Shinde, J. Appl. Phys. **109**, 083504 (2011).
[18] H. Stillrich, C. Menk, R. Frömter, and H. P. Oepen, J. Appl. Phys. **105**, 07C308 (2009).
[19] G. Winkler, A. Kobs, A. Chuvilin, D. Lott, A. Schreyer, and H. P. Oepen, J. Appl. Phys. **117**, 105306 (2015).
[20] K. Kang, Y. K. Koh, C. Chiritescu, X. Zheng, and D. G. Cahill, Rev. Sci. Instrum. **79**, 114901 (2008).
[21] D. G. Cahill, Rev. Sci. Instrum. **75**, 5119 (2004).
[22] R. M. Costescu, M. A. Wall, and D. G. Cahill, Phys. Rev. B **67**, 054302 (2003).
[23] M. Kochsiek, Metrologia **18**, 153 (1982).
[24] F. E. Jones and R. M. Schoonover, *Handbook of Mass Measurement* (CRC Press, Boca Raton, FL, 2002).
[25] P. J. Cumpson and M. P. Seah, Metrologia **33**, 507 (1996).
[26] G. T. Hohensee, R. Wilson, and D. Cahill, Nat. Commun. **6**, 6578 (2015).
[27] Y. K. Koh, S. L. Singer, W. Kim, J. M. O. Zide, H. Lu, D. G. Cahill, A. Majumdar, and A. C. Gossard, J. Appl. Phys. **105**, 054303 (2009).
[28] J. Kimling, J. Kimling, R. B. Wilson, B. Hebler, M. Albrecht, and D. G. Cahill, Phys. Rev. B **90**, 224408 (2014).
[29] M. Hu, P. Keblinski, and P. K. Schelling, Phys. Rev. B **79**, 104305 (2009).
[30] M. D. Losego, M. E. Grady, N. R. Sottos, D. G. Cahill, and P. V. Braun, Nat. Mater. **11**, 502 (2012).
[31] G.-M. Choi, C.-H. Moon, B.-C. Min, K.-J. Lee, and D. G. Cahill, Nat. Phys. **11**, 576 (2015).
[32] R. B. Wilson, B. A. Apgar, W.-P. Hsieh, L. W. Martin, and D. G. Cahill, Phys. Rev. B **91**, 115414 (2015).
[33] J. Chen, G. Zhang, and B. Li, J. Appl. Phys. **112**, 064319 (2012).
[34] M. Albrecht, G. Hu, I. L. Guhr, T. C. Ulbrich, J. Boneberg, P. Leiderer, and G. Schatz, Nat. Mater. **4**, 203 (2005).
[35] R. B. Wilson and D. G. Cahill, Nat. Commun. **5**, 5075 (2014).
[36] Z. Q. Qiu and S. D. Bader, Rev. Sci. Instrum. **71**, 1243 (2000).
[37] S. Fiedler, H. Stillrich, and H. P. Oepen, J. Appl. Phys. **102**, 083906 (2007).